Journal of Power Sources 195 (2010) 5071–5080

Contents lists available at ScienceDirect

Journal of Power Sources

journal homepage: www.elsevier.com/locate/jpowsour

Experiment-driven electrochemical modeling and systematic parameterization for a lithium-ion battery cell

Alexander P. Schmidt[a,*], Matthias Bitzer[b], Árpád W. Imre[a], Lino Guzzella[c]

[a] Robert Bosch GmbH, Corporate Research, Electric Vehicle - System & Components, Robert-Bosch-Strasse 2, D-71701 Schwieberdingen, Germany
[b] Robert Bosch GmbH, Corporate Research, Control Theory, Robert-Bosch-Strasse 2, D-71701 Schwieberdingen, Germany
[c] Institute for Dynamic Systems and Control (IDSC), ETH Zurich, Sonneggstrasse 3, CH-8092 Zurich, Switzerland

ARTICLE INFO

Article history:
Received 8 September 2009
Received in revised form 18 January 2010
Accepted 14 February 2010
Available online 20 February 2010

Keywords:
Extended non-isothermal single particle model
SOC-dependent diffusivity
Lumped parameter system
Combined parameter analysis and identification
Fisher-information matrix
Sensitivity analysis

ABSTRACT

This paper presents a novel electrochemical lithium-ion cell model which can be used in battery control units. Based on classical single-particle approaches, a lumped-parameter nonlinear model is developed that is able to predict accurately the terminal voltages for arbitrary loads, and even for potentiostatic operation. The key points are: (1) an incorporation of the electrolyte potential, (2) a modal decomposition of the partial differential equation of the liquid phase lithium-ion concentration, (3) a correct handling of the SOC-dependent diffusivity in the insertion materials of both electrodes, and (4) a consideration of temperature-dependent kinetic processes. A combined parameter analysis and identification is successfully applied for the parameterization of the model. Using a Fisher-information matrix approach in combination with a sensitivity analysis, the identifiability of each parameter is estimated in dependence on the measurement information. Using this information, it is possible to choose a small number of relevant experiments which are sufficient to fully parameterize the model.

1. Introduction

Throughout the ongoing discussion on vehicle emissions, hybrid or full electric drivetrains have increasingly come into the spotlight. Currently, lithium-ion batteries are regarded as the most promising electrical energy storage technology due to their high energy and power density [1,2]. The harsh demands by the automobile industry concerning safety and lifetime requirements slow down a wider introduction of their series production for drivetrains. Thus, the state of charge (SOC), the terminal voltage, and the temperature have to be accurately predicted and monitored. In this context, the usage of electrochemical battery models is desirable. They provide excellent capabilities for predicting the cell's short-term behavior (charge/discharge characteristics) and incorporate inherent physical parameters. This enables the extension of the models by physics-based aging effects, e.g. by the fading of capacity and power [3].

Originally, the electrochemical modeling of secondary lithium-ion batteries was based on the theories of porous electrodes and concentrated solutions [4]. These considerations typically lead to distributed parameter systems, which have been investigated by various authors [5–14]. Such a model can be reduced to a so-called single-particle (SP) model first proposed in [15]. However, the distributed model as well as the SP model failed in the accurate prediction of the input/output behavior at high current rates and/or high temperature variations.

This work is focussed on the development of an easy-to-handle extended lumped parameter model based on the named single particle approach. The later on presented model accurately reproduces the input/output behavior for the complete operating range of a commercially available high-power lithium-ion cell. The data evaluation of cycling experiments motivated the newly proposed model extensions. A quick and reliable identification scheme for the full parameter set is presented as well. This issue is addressed by the so-called combined parameter analysis and identification [16–18]. Within this method, the Fisher-information matrix is utilized to assess the identifiability of single parameters in dependence of the information content of a single measurement. Moreover, the Fisher-information matrix accounts for the expected variances and output sensitivities of the parameters. This framework is successfully applied to verify the new model extensions.

* Corresponding author. Tel.: +49 711 81134050; fax: +49 711 81151824787.
E-mail addresses: alexander.schmidt7@de.bosch.com (A.P. Schmidt), matthias.bitzer2@de.bosch.com (M. Bitzer), arpad.imre@de.bosch.com (Á.W. Imre), lguzzella@ethz.ch (L. Guzzella).
URL: http://www.idsc.ethz.ch (L. Guzzella).

0378-7753/$ – see front matter © 2010 Elsevier B.V. All rights reserved.
doi:10.1016/j.jpowsour.2010.02.029

Table 1
List of symbols.

Symbol	Description
a_j, b_j, d_j	Time-varying coefficients (mol m^{-3})
$a_{s,j}$	Active surface area (m^2)
$c_{1/2,j}$	Bulk lithium-ion concentration (mol m^{-3})
$c_{1,s,j}$	Surface lithium-ion concentration (mol m^{-3})
$c^*_{2,k}$	Temporal mode of c_2 (−)
D_F	Diagonalized Fisher-information matrix (−)
E	Expectation value (−)
$f_\pm$	Mean molar salt activity (m^2 s^{-1})
F_{info}	Fisher-information matrix (−)
$i_{0,j}$	Exchange current density (A m^{-2})
$i_{1/2}$	Cell internal current (A m^{-2})
I	External load current (A m^{-2})
j_j	Reaction rate (mol m^{-2} s^{-1})
N	Total number of data points (−)
N_θ	Total number estimated parameters (−)
p	Probability density function (−)
$q_{1/2,j}$	Lithium-ion flux (mol m^{-3})
r	Independent variable, radial direction (−)
R_j	Radius of active particle (m)
$R_{SEI,j}$	SEI film resistance (Ω m)
$S_{x/y}$	Sensitivity w.r.t. parameters (−)
t	Time (s)
t^0_+	Transference number (−)
T	Cell temperature (K)
T_{corr}	Temperature correction for kinetics (−)
T_∞	Ambient temperature (K)
u	Input magnitude (−)
U	Terminal voltage of the cell (V)
U_{ocp}	Open circuit potential (V)
V	total number of experiments
$\mathbf{x}$	State variable vector (−)
$\mathbf{y}$	Output vector (−)
z	Independent variable, across cell sandwich (−)
Z	Transformation matrix (−)
γ	Variance boundary for identification (−)
Γ_j	Spatial domain in z (−)
η_j	Surface overpotential (V)
$\lambda_{\min}$	Minimum eigenvalue of F_{info} (−)
$\Phi_{1/2,j}$	Electrochemical potential (V)
σ	Variance (−)
$\boldsymbol{\theta}$	Parameter vector (−)
$\hat{\theta}$, θ^*	Estimated parameter, true parameter (−)
τ_j	Diffusion time constant (s)

2. State-of-the-art electrochemical battery modeling

In this section, the physical background, modeling assumptions, as well as the single particle approach for lithium-ion intercalation cells are summarized. Symbols and indices employed below are listed in Tables 1 and 2.

Table 2
List of indices.

Index	Description
$\overline{(.)}$	Volume averaged magnitude
1	Related to the solid active material
2	Related to the electrolyte phase
a	Active material of the anode
c	Active material of the cathode
cc	At the current collector of the anode
i	Index of a certain parameter
j	General index for spatial cell segment
k	Temporal mode number
l	Electrolyte phase
m	General index for a phase segment
n	Index of a uncorrelated parameter
s	Related to the separator
w	Index of a certain data point
ξ	Index of a certain measurement
υ	Index of a certain output (−)

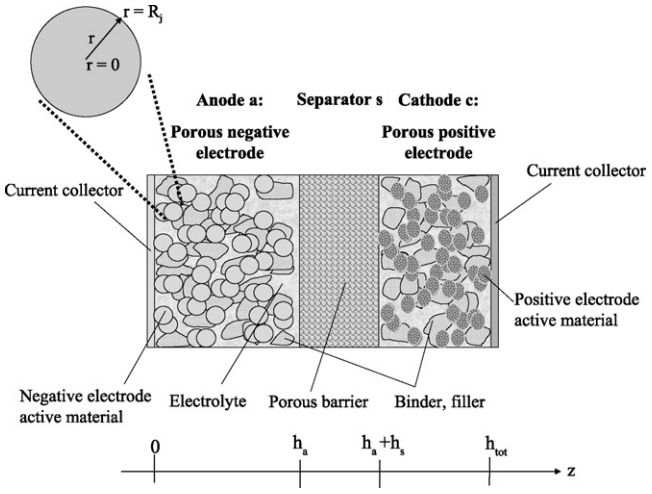

Fig. 1. Schematic drawing of a lithium-ion dual intercalation cell.

2.1. Physical background and first principle modeling

An electrochemical dual intercalation cell according to [4] contains two electrically separated porous electrodes, see Fig. 1. Whereas the anode is predominantly a graphite derivative, there exist numerous metal oxide materials for the cathode, see e.g. [19]. Typically, both electrodes consist of a grain structure of quasi-spheric active particles in a μm scale. Lithium ions are stored in vacant sites of the actual crystal lattice of these active particles. A detailed discussion on intercalation electrodes can be found in [4] for instance. The difference in the potentials of the two electrodes determines the terminal voltage of the cell. The concentration of ions in the insertion materials correlates with the state of charge (SOC). The process of charge and discharge is started by the closure of the outer electrical circuit. The lithium ions are transported by diffusion inside the active particles along the r-axis, see Fig. 1. The ions carrying the charge pass through the particle–electrolyte interface according to the Butler–Volmer kinetics. Meanwhile, the electrons are transported to the current collectors. Subsequently, the lithium ions travel via diffusion and migration – dissolved in the electrolyte – through the separator to the backplate electrode along the z-axis, as shown in Fig. 1. Due to the mainly ohmic losses, the cell consumes parts of the stored energy by dissipation, resulting in a self-heating phenomenon. For a better understanding of the following text, a distributed parameter reference model [5] is given in Appendix A.

2.2. The single particle (SP) model

In order to develop an application-oriented electrochemical cell model, a so-called single particle model was suggested in [15]. In this context, the electrolyte phase is neglected and each electrode is replaced by only one representative active particle. A form ansatz as outlined in [11] and [20] for the approximate solution of the partial differential equation (PDE) of the solid-phase lithium-ion concentration $c_{1,j}(r, t)$, see Eq. (A.1), paved the way for a lumped parameter model. The volume-averaged quantities solid-phase flux $\bar{q}_{1,j}(t)$ and solid-phase lithium ion concentration $\bar{c}_{1,j}(t)$ are introduced in order to preserve the physical meaning of the state variables. The result is a set of two ordinary differential equations (ODEs) for $\bar{q}_{1,j}(t)$ and $\bar{c}_{1,j}(t)$, i.e.

$$\begin{aligned} \frac{d\,\bar{c}_{1,j}}{dt} &= -3\frac{j_j}{R_s}, \\ \frac{d\,\bar{q}_{1,j}}{dt} &= -30\frac{D_{s,j}}{R_j^2}\bar{q}_{1,j} - \frac{45}{2R_j^2}j_j, \end{aligned} \tag{1}$$

and one algebraic equation for the particle surface concentration $c_{1,s,j}$ at $r = R_j$, i.e.

$$c_{1,s,j} = \bar{c}_{1,j} + \frac{8R_j}{35}\bar{q}_{1,j} - \frac{R_j}{35D_{s,j}}j_j, \tag{2}$$

where $D_{s,j}$ is the solid phase diffusion coefficient, R_j is the particle radius, and j_j is the reaction rate according to Eq. (A.6).

3. New extensions to the SP model

The extensions presented below have been introduced to improve the model prediction quality. First, in Section 3.1 an easy-to-handle set of equations for the impact of the anodic electrolyte potential to the terminal voltage of the cell is derived. Section 3.2 outlines the necessity for variable diffusion speeds in the solid insertion materials with respect to the SOC. In Section 3.3, a simple thermal model is derived. It newly accounts for the temperature dependence of the kinetic [22] as well as of the ion transport processes. Finally, in Section 3.4 the model equations are presented in a nonlinear state space form.

3.1. Approximate solution for the electrolyte potential and the electrolyte lithium-ion concentration

In the original SP model as introduced in Section 2.2 the electrolyte potential $\Phi_{2,j}$ is completely neglected. But, for high current rates the charge transfer of lithium-ions across the solid-electrolyte interface and thus, the terminal voltage U of the lithium-ion cell is essentially affected by $\Phi_{2,j}$. Therefore, the following approximate solution for the electrolyte potential $\Phi_{2,j}$ is applied to the SP model. For a detailed discussion on the mathematical relation of the cell-internal potentials and the terminal voltage, the reader is referred to Appendixes A and B.

The graphitic anode material of the considered cell exhibits a low potential $\Phi_{1,a}$ vs. Li/Li$^+$ in the range of 0.0–0.1 V. Simulations of the distributed reference model according to Eqs. (A.1)–(A.7) by the author of [23] have shown that the electrolyte potential $\Phi_{2,j}$ reaches similar voltage values for high current rates. However, the potential $\Phi_{1,c}$ of more than 4 V vs. Li/Li$^+$ of the metal oxide cathode is always far beyond this value. Hence, the profile across the cell layers of the electrolyte potential $\Phi_{2,j}$ is reduced to the relevant boundary value at the current collector of the anode, compare to Fig. 1. This is achieved by solving the corresponding partial-algebraic model equation, i.e.

$$0 = -\frac{\partial\Phi_{2,j}}{\partial z} - \frac{i_{2,j}}{\kappa} + RT\,\zeta\left(1 + \frac{\partial \ln f_j}{\partial \ln c_{2,j}}\right)\frac{\partial}{\partial z}(\ln c_{2,j}), \tag{3}$$

see also Eq. (A.4). The solution of Eq. (3) for $z = 0$, i.e. $\Phi^{cc}_{2,a}(t) := \Phi_{2,a}(z = 0, t)$ yields

$$\Phi^{cc}_{2,a}(t) = \frac{1}{\kappa}\cdot w \cdot h_{\text{tot}} \cdot I(t) + \frac{RT}{F}\beta[\ln c_{2,a} - \ln c_{2,c}] \tag{4}$$

with $w = 1/2\,h_a + h_s + 1/2\,h_c$ and $\beta = (1 + \partial \ln f_{\pm}/\partial \ln c_{2,j})(1 - t^0_+) = \text{const}$.

The electrolyte potential obviously depends on the lithium-ion concentration. Thus, the underlying lithium-ion concentration distribution $c_{2,j}(z, t)$ in the electrolyte is approximated by a single ODE. This ODE accounts for the time coefficient of the dominant mode together with its corresponding spatial eigenfunction of the respective PDE [21]. The procedure is as follows. The electrolyte concentrations $c_{2,a} = c_{2,a}(0, t)$, $c_{2,c} = c_{2,c}(h_{\text{tot}}, t)$ in Eq. (4) are determined by solving the corresponding PDE in Eq. (A.2), i.e.

$$\frac{\partial c_2}{\partial t} = \frac{1}{\epsilon}D\frac{\partial^2 c_2}{\partial z^2} + \frac{\zeta}{\epsilon}\frac{\partial i_2}{\partial z}, \tag{5}$$

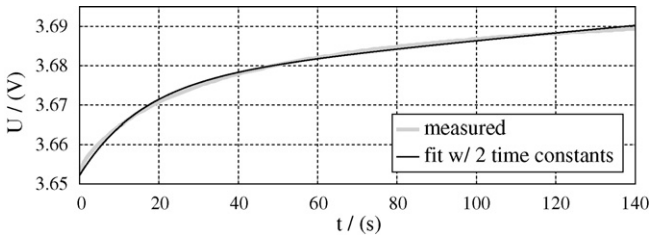

Fig. 2. Relaxation of the cell's terminal voltage after a small load current $I(t) = C/60$ is switched off, in comparison to a fit with two time constants τ_a and τ_c.

by means of a modal transform as presented by the author of [21], see Appendix C. Using the inverse modal transform the solution of Eq. (5) can be expressed by the infinite sum

$$c_2(z, t) \approx \sum_{k=0}^{\infty} c^*_{2,k}(t)\cdot\varphi_k(z) \tag{6}$$

with the temporal modes $c^*_{2,k}(t)$ Eq. (C.5) and the spatial eigenfunctions $\varphi_k(z)$, see [21]. For Eq. (5) in conjunction with its boundary conditions (see Appendix A), it turns out that only the first two modes $k = 0, 1$ yield an appreciable contribution to the sum in Eq. (6). Furthermore, the mode $k = 0$ degenerates to $dc^*_{2,0}/dt = 0$. Finally, the dynamic contribution of $c_{2,j}(z, t)$ to Eq. (4) can be reduced to the first mode $c^*_{2,1}$ which reads as:

$$\frac{dc^*_{2,1}}{dt} = \lambda_k c^*_{2,1}(t) + \frac{\zeta}{\epsilon}i^*_{2,1}(t). \tag{7}$$

The derivation of Eq. (7) is discussed in detail in Appendix C as well as the modal transform framework.

3.2. SOC-dependent apparent diffusion in the solid

The relaxation in the terminal voltage of a lithium-ion cell that is observed after a small load current is switched off is typically a superposition of two relaxation regimes with the time constants τ_a and τ_c, see Fig. 2. Usually τ_c is about one order of magnitude larger than τ_a. They correspond to anodic and cathodic solid diffusion coefficients $D_{s,j}$ which vary with respect to the state of charge $\overline{SOC}_j$ averaged over the particle volume (see Appendix B for a discussion on SOC definitions). The following correlation yields a good agreement of the model with measurement data of arbitrary load profiles:

$$D_{s,j} = \frac{D_{s,j,ref}}{2}[1 + \tanh(-\gamma_j(\overline{SOC}_j - \delta_j))], \tag{8}$$

where $D_{s,j,ref}$ is the standard value at $\overline{SOC}_j = 0$ and $T_\infty = 298$ K. The values γ_j and δ_j are constant form coefficients. They have been determined using the parameter identification method outlined in Section 4. In contrast to recently publicated results [24], here, the diffusivity $D_{s,c}$ of the cathode decreases gradually with increasing $\overline{SOC}_c$ in the whole $\overline{SOC}_c$ range, as shown in Fig. 3. This can be explained by the fact that the cell investigated contains a cathode consisting of two different insertion materials.

According to [25], the issue of a (volatile) change in the diffusion velocity can be interpreted as an alteration of the underlying diffusion mechanism. Another possible explanation for the change in the relaxation time constant is that the ion saturation of tiny particles shifts the average diffusion lengths (R_j) to larger values since there always exists a certain distribution of particle sizes in the electrodes. To verify the assumed correlation of the SOC-dependent solid state diffusivity Eq. (8) and the voltage relaxation time constants (as depicted in Fig. 2), the Einstein–Smoluchowski relation $D_{s,j} = R_j^2/(6\,\tau_j)$ as described in [25] has been applied to the voltage

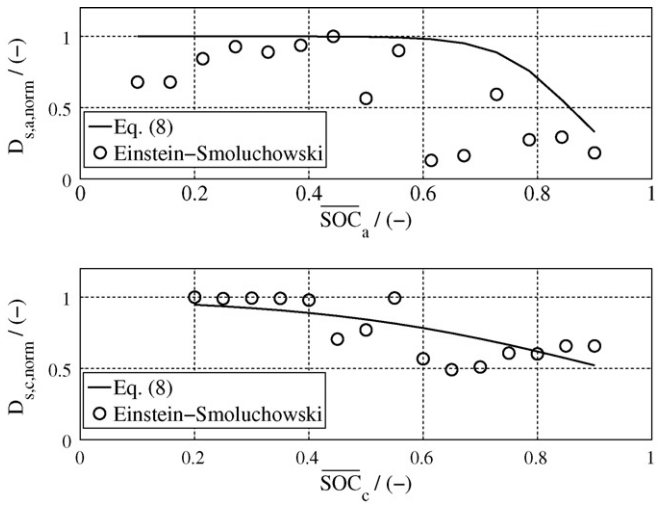

Fig. 3. Variation of the diffusion coefficients $D_{s,j}$ as a function of $\overline{SOC}_j$. Comparison between the Einstein–Smoluchowski relation, applied to the voltage relaxation, and the form ansatz Eq. (8) identified for arbitrary current loads.

relaxation data of the cell, see also Fig. 3. For this verification, the battery was partially discharged by a constant current of $I = C/60$, followed by rest phases with $I = 0$.

3.3. Balance equation for the temperature considering radiation

The consideration of heat generation within this model is reduced to ohmic heating P_{el} as the only source term. Other source terms such as the reaction heat outlined for instance in [26], could not be identified during cycling experiments. Regarding the heat losses, the radiation heat transfer $\dot{Q}_{\text{rad}}$ as it is described in [27,28] was found to be in the same order of magnitude as convection $\dot{Q}_{\text{conv}}$. Hence, the first law of thermodynamics for closed systems can be applied which yields

$$\frac{dT}{dt} = \frac{A_s}{\rho v_c C_p}\left[P_{el} + \dot{Q}_{\text{conv}} + \dot{Q}_{\text{rad}}\right], \tag{9}$$

with $P_{el} = A_{el}/A_s\,\Delta\eta\, I$, $\dot{Q}_{\text{conv}} = h_{tc}(T_\infty - T)$, and $\dot{Q}_{\text{rad}} = \epsilon_{\text{rad}}\,\sigma_B(T_\infty^4 - T^4)$. Here, $\Delta\eta = \eta_c - \eta_a$ is the effective overpotential according to Eq. (A.7).

3.3.1. Arrhenius-type temperature correction for the reaction kinetics

The cell temperature Eq. (9) is utilized to account for speed variations of the reaction kinetics and transport processes, i.e. $D_{s,j} = D_{s,j}(T_{\text{corr}})$, $i_{0,j} = i_{0,j}(T_{\text{corr}})$, and $\kappa = \kappa(T_{\text{corr}})$. This is reached by an Arrhenius-type dimensionless correction term as outlined in [29] according to

$$T_{\text{corr}}(T(t)) = \exp\left[\frac{E_{0,m}}{R}\left(\frac{1}{T_{\text{ref}}} - \frac{1}{T(t)}\right)\right], \tag{10}$$

with $E_{0,m}$ being the activation energy of the respective domain $m \in a, c, l$ [1] at the reference temperature $T_{\text{ref}} \approx 298$ K, see e.g. [29].

3.4. Nonlinear model structure

From a control-theoretical point of view, the proposed system Eqs. (1)–(10) represents a nonlinear state space model of the form

$$\dot{\boldsymbol{x}}(t) = \boldsymbol{f}(\boldsymbol{x}(t), \boldsymbol{\theta}, T_\infty(t), u(t)), \quad t > 0, \tag{11}$$

[1] Here, l denotes for the liquid phase and is thus relevant for κ.

Table 3
Fixed design specific parameters.

Parameter	Description
T_{ref}	Reference temperature (K)
h_a	Thickness of negative electrode (m)
h_s	Thickness of separator (m)
h_c	Thickness of positive electrode (m)
C_a	Coulombic capacity of negative mat. (mAh g^{-1})
$C_{c,a}$	Coulombic capacity of positive mat. a (mAh g^{-1})
$C_{c,b}$	Coulombic capacity of positive mat. b (mAh g^{-1})
ρ_a	Density of neg. insertion mat. (kg m^{-3})
$\rho_{c,a}$	Density of pos. insertion mat. a (kg m^{-3})
$\rho_{c,b}$	Density of pos. insertion mat. b (kg m^{-3})
A_s	Cell surface area (m^2)
ρ	Overall density of cell (kg m^{-3})
v_c	Cell volume (m^3)
C_p	Heat capacity of cell material (J kg^{-1} K^{-1})
A_{el}	Electrode plate area (m^2)
$\text{vol}_{c,a}$	Vol. fraction of positive active mat. a (–)

$$\boldsymbol{y}(t, \boldsymbol{\theta}) = \boldsymbol{h}(\boldsymbol{x}(t), \boldsymbol{\theta}, T_\infty(t), u(t)), \quad t \geq 0. \tag{12}$$

In this context, the system's state vector is defined by $\boldsymbol{x}(t) = [\bar{q}_a(t), \bar{q}_c(t), \bar{c}_a(t), \bar{c}_c(t), T(t), c^*_{2,1}(t)]^T$, the scalar input by $u(t) = I(t)$, and the parameter vector by $\boldsymbol{\theta}$. The output vector is found as $\boldsymbol{y}(t, \boldsymbol{\theta}) = \left[T(t), U(\boldsymbol{x}(t), \boldsymbol{\theta})\right]^T$. The cell terminal voltage $U(\boldsymbol{x}(t), \boldsymbol{\theta})$ is obtained by a reformulation of the Butler–Volmer kinetics Eq. (A.6) as described in Appendix B. The model states $\bar{c}_a(t)$ and $\bar{c}_c(t)$ are measures for the SOC, see also Appendix B for a detailed discussion on that issue. The ambient temperature $T_\infty(t)$ is considered as a time-variant parameter since it can be adjusted using an experimental set-up with a climate chamber.

The complete set of parameters $\boldsymbol{\theta}$ of Eqs. (11) and (12) can be found in Tables 3–6. They are classified into fixed geometric and design-specific parameters, see Table 3, physical constants, see Table 4, thermodynamic, kinetic, as well as internal parameters, see Table 5, and finally semi-empiric parameters, see Table 6. The parameters of Tables 3 and 4 are assumed to be known a priori. Below, the proper identification of 33 thermodynamic, kinetic, and semi-empiric parameters will be dealt with.

Table 4
Physical constants.

Parameter	Value	Description
F	96,485	Faraday's constant (C mol^{-1})
σ_B	5.67e−08	Stefan–Boltzmann constant (W m^{-2} K^{-4})
R	8.314	Ideal gas constant (J mol^{-1} K^{-1})

Table 5
Thermodynamic, kinetic and internal parameters.

Parameter	Description
$E_{0,a}$	Activation energy of anodic kinetics (J)
$E_{0,c}$	Activation energy of cathodic kinetics (J)
$E_{0,l}$	Activation energy of electrolyte kinetics (J)
R_a	Radius of neg. insertion mat. (m)
R_c	Effective radius of pos. insertion mat. (m)
$D_{s,a}$	Diff. coeff. of neg. insertion mat. (m^2 s^{-1})
$D_{s,c}$	Diff. coeff. of pos. insertion mat. (m^2 s^{-1})
ϵ_a	Porosity of negative insertion material (–)]
ϵ_c	Porosity of positive insertion material (–)
rka_a	Reaction rate constant for neg. reaction (–)
rka_c	Reaction rate constant for pos. reaction (–)
κ	Conductivity of electrolyte phase (S m^{-1})
D_{el}	Electrolyte diffusion coeff. (m^2 s^{-1})
h_{tc}	Convective heat transfer coeff. (W m^{-2} K^{-1})
ϵ_{rad}	Heat rad. transf. coeff. for cell casing (–)
c_0	Avg. electrolyt. concentration of Li$^+$ (mol m^{-3})

Table 6
Semi-empiric parameters.

Parameter	Description
β	Coefficient for electrolyte concentration (−)
$a_{c,i}$	Coefficients for cathode OCP (−)
$a_{a,i}$	Coefficients for anode OCP (−)
γ_a	Coefficient for anode diffusion (−)
γ_c	Coefficient for cathode diffusion (−)
δ_a	Coefficient for anode diffusion (−)
δ_c	Coefficient for anode diffusion (−)

4. Structured model parameterization

The identification of the model parameters $\boldsymbol{\theta}$ in Eqs. (11) and (12) according to Tables 5 and 6 is approached by means of a nonlinear optimization problem, as specified in Section 4.1. In order to improve the estimation quality, the optimization is further performed in combination with a parameter analysis [17] discussed in Section 4.2.

4.1. The nonlinear optimization problem of parameter estimation

The nonlinear optimization problem for the parameter identification is set up by means of a least-squares framework. Therefore, the objective function L can be derived from the Maximum-Likelihood method [30], i.e.

$$\min L(\boldsymbol{\theta}) = \min \frac{1}{2}\sum_{\upsilon=1}^{2}\sum_{\xi=1}^{V}\sum_{w=1}^{N}\frac{(\hat{y}_\upsilon(t_w) - y_\upsilon(t_w,\boldsymbol{\theta}))^2}{\sigma_\upsilon^2(\boldsymbol{\theta})}, \tag{13}$$

in dependence of the data points $\hat{y}_\upsilon(t_w)$, $w = 1,\ldots,N$ of $\xi = 1,\ldots,V$ experiments, and the model outputs $y_\upsilon(t_w,\boldsymbol{\theta})$, $\upsilon = 1,2$ in Eq. (12). The covariance estimates $\sigma_\upsilon^2(\boldsymbol{\theta})$ [31] for each ξ are determined according to

$$\sigma_\upsilon^2(\boldsymbol{\theta}) = \frac{1}{N - N_\theta}\sum_{w=1}^{N}(\hat{y}_\upsilon(t_w) - y_\upsilon(t_w,\boldsymbol{\theta}))^2, \tag{14}$$

where N_θ is the number of parameters. Additional constraints can be incorporated as a penalty in the objective function $L(\boldsymbol{\theta})$.

4.2. The method of combined analysis and identification

In this section, an algorithm for the analysis of the identifiability of the parameters [17,31] is introduced. It is applied to the parameter estimation problem of secondary lithium-ion cells for the first time. This approach excludes unidentifiable, i.e. insensitive parameters from the optimization in dependence of the respective measurement information. Thus, the overall identification quality of the remaining parameters is increased.

4.2.1. Parameter analysis based on Fisher-information matrix and parameter sensitivities

Considering the parameter vector $\boldsymbol{\theta}$ of the system Eqs. (11) and (12), the deviation of the estimate $\hat{\boldsymbol{\theta}}$ from the true value $\boldsymbol{\theta}^*$ can be measured by the covariance matrix $\operatorname{cov}\hat{\boldsymbol{\theta}}$ [32]. Its lower bound is given by means of the Cramér–Rao inequality [33,34]

$$\operatorname{cov}\hat{\boldsymbol{\theta}} \geq F_{\text{info}}^{-1}(\boldsymbol{\theta}^*) \tag{15}$$

with the inverse Fisher-information matrix F_{info}^{-1}. It is defined as [32,34]

$$F_{\text{info}}(\boldsymbol{\theta}^*) = E\left\{\frac{\partial^2}{\partial\boldsymbol{\theta}^2}V_p(\boldsymbol{\theta})\right\}\Big|_{\boldsymbol{\theta}=\boldsymbol{\theta}^*} \tag{16}$$

and denotes the expectation value $E\{\cdot\}$ of the expression $V_p = -\ln p(\boldsymbol{\theta})$ for the true parameter set $\boldsymbol{\theta}^*$, with $p(\boldsymbol{\theta})$ representing the probability density function [30,32]. Practically, the Fisher-information matrix can be computed by

$$F_{\text{info}}(\boldsymbol{\theta}) = \sum_{w=1}^{N} S_y^T|_w \underbrace{\begin{bmatrix} \frac{1}{\sigma_{1,w}^2} & & 0 \\ & \ddots & \\ 0 & & \frac{1}{\sigma_{N_\theta,w}^2} \end{bmatrix}}_{C_{t,w}^{-1}} S_y|_w, \tag{17}$$

where $S_y|_w$ are the output sensitivities of the parameters and $C_{t,w} = \operatorname{diag}(\sigma_{t,w}^2)$ is the covariance matrix of the measurements. State and output sensitivities are defined as

$$S_x = \frac{\partial\boldsymbol{x}}{\partial\boldsymbol{\theta}}, \quad S_y = \frac{\partial\boldsymbol{y}}{\partial\boldsymbol{\theta}}. \tag{18}$$

Both are calculated using the sensitivity differential equations (SDEs) [35,36] according to

$$\dot{S}_x = \frac{\partial\boldsymbol{f}}{\partial\boldsymbol{x}}S_x + \frac{\partial\boldsymbol{f}}{\partial\boldsymbol{\theta}}, \qquad t > 0, \quad S_x(0) = \frac{\partial\boldsymbol{x}_0}{\partial\boldsymbol{\theta}} \tag{19}$$

$$S_y = \frac{\partial\boldsymbol{h}}{\partial\boldsymbol{x}}S_x + \frac{\partial\boldsymbol{h}}{\partial\boldsymbol{\theta}}, \qquad t \geq 0. \tag{20}$$

The Fisher-information matrix Eq. (17) is now utilized for the analysis of the contribution of individual parameters θ_i to the estimation quality of the nonlinear optimization problem Eq. (13), see [31] for instance. In order to employ the Fisher-information matrix Eq. (17) for the assessment of the identifiability of the parameters, the Cramér–Rao inequality Eq. (15) is transformed to

$$cov(\tilde{\boldsymbol{\theta}} - \boldsymbol{\theta}^*) \geq D_F^{-1} = diag\left(\frac{1}{\lambda_n}\right) \tag{21}$$

with $\tilde{\boldsymbol{\theta}}$ denoting for the vector of uncorrelated parameters in the transformed space and the diagonalized Fisher-information matrix $D_F = Z^T F_{\text{info}} Z$. The identifiability of each untransformed parameter is then measured by its contribution to a respective transformed variance $\tilde{\sigma}_n^2$ whose lower boundary is estimated by the eigenvalues of D_F, i.e.

$$\tilde{\sigma}_n^2 \geq \frac{1}{\lambda_n}. \tag{22}$$

For a detailed discussion on the presented parameter analysis algorithm the interested reader is referred to [17].

4.2.2. Parameter group assignment

The consideration of insensitive parameters with large variances in the optimization problem Eq. (13) is known to decrease substantially the overall estimation quality [17,31]. Therefore, the parameter analysis together with a corresponding group assignment [17,31] eliminates insensitive parameters θ_i from the identification step. Only those parameters whose variances are below a fixed boundary are identified together [17]. The first group, representing the optimization variables during the identification step, is determined as follows [17,18].

The parameter θ_i, which accounts for the largest share to the largest transformed variance $\sigma_{n,\max}^2$ and thus, for the smallest eigenvalue $\lambda_{\min}$ of the diagonalized Fisher-information matrix D_f is excluded from the optimization Eq. (13) if $\lambda_{\min}$ violates the condition

$$\sqrt{\frac{1}{\lambda_{\min}}} \leq \gamma \tag{23}$$

with the fix boundary value γ. The untransformed Fisher-information matrix F_{info} is then reduced by the row and the column containing to the most uncertain parameter θ_i. This is achieved by examining the eigenvector that belongs to $\lambda_{\min}$. The just outlined procedure is repeated until all variances σ_n^2 are smaller than γ, which corresponds to the fixing of the first group. The same procedure is then applied to all recently excluded parameters until every single parameter θ_i of the whole set is assigned to a certain group. For a detailed description of the grouping algorithm the reader is referred to [31]. After obtaining an optimization result for parameters within the first group, the analysis and the group assignment are repeated. The termination of the entire algorithm [17,18,31] is reached by means of an unchanged set $\boldsymbol{\theta}_{1st}$, which is equivalent to the fact that all parameters which are identifiable according to Eq. (23) have been estimated. Thus, the information content of the underlying measurement data has been completely exploited. To achieve further improvements in both the number of identifiable parameters $\boldsymbol{\theta}_{1st}$ and the overall estimation quality, additional measurements are necessary. It is worth mentioning that these can be obtained with a respective design of experiments [17,31,37–41].

5. Application of the parameterization scheme to the model and results

The parameterization of the proposed cell model according to Section 3 by use of the combined analysis and identification method as presented in Section 4 is discussed. Therefore, additional technical prerequisites and the parameterization itself are outlined in Section 5.1. Subsequently, the achieved prediction quality of the proposed model Eqs. (11) and (12) for realistic operating conditions is discussed in Section 5.2 by comparing the model to the measurement data of a cell. Currents $I(t)$ are given in terms of the commonly used C-rate [19].

5.1. Application of the combined parameter analysis and identification

First, the simultaneous solution of the system and the sensitivity equations is outlined. The proper choice of experiments [39] is then discussed with respect to the identifiability of parameters.

5.1.1. Simultaneous solution of the model and the sensitivities

For a given measurement the variances σ_v^2 are computed according to Eq. (14). Within this work the state-dependent Jacobians of the system Eqs. (11) and (12) have been derived analytically using the computer-algebra tool Mathematica [42]. Both the SDEs Eqs. (19) and (20) and the system Eqs. (11) and (12) are then implemented in the simulation environment Matlab/Simulink [43] and are solved simultaneously. The simulation time[2] for a set of experiments as outlined in the next section is in the range of a few seconds for the pure model Eqs. (11) and (12) and in the range of $1-3$ minutes for the sensitivities Eqs. (19) and (20). The initial set $\boldsymbol{\theta}_{init}$ is taken in part from the corresponding literature [3–14,19,20,24,44–50] and is partially found by best practice. The choice of the variance boundary γ represents one degree of freedom. It was set to $\gamma = 0.15$, as proposed in [17]. The optimization itself is conducted using the Matlab-based tool MOPS (Multi-Objective Parameter Synthesis) [51]. Its included pattern search algorithm [52] has been employed.

[2] On a PC with an Intel Centrino Duo processor.

Table 7
Experiments used for the parameter identification of the model.

Exp. ξ	$\vartheta_\xi/(h)$	$\lvert\hat{I}_\xi(t)\rvert/(C)$	$\widehat{\Delta T}_{\infty,\xi}(t)/(K)$	$\widehat{\Delta T}_\xi(t)/(K)$
1	100	1/60	≈ 0	≈ 0
2	1.25	1.8	32	32
3	1.25	0.5	10	10
4	3.61	16	≈ 0	≈ 62
5	3.89	8	≈ 0	≈ 40

5.1.2. Model parameterization with five experimental data sets

The cell was stimulated with the input signals $u_\xi(t) = I_\xi(t)$, $\xi = 1, \ldots, 5$, $t \in \vartheta_\xi = [0, t_{end,\xi}]$ and the manipulated ambient temperature signals $T_{\infty,\xi}(t)$ of the climate chamber. The index ξ represents the respective experiment. The experiments $\xi = 1, 4, 5$ were conducted with constant ambient temperature, while it was varied for the experiments $\xi = 2, 3$. The five experiments can be characterized according to their duration ϑ_ξ, the maximum applied current $\lvert\hat{I}_\xi(t)\rvert$, the maximum applied variation of ambient temperature $\widehat{\Delta T}_{\infty,\xi}(t)$, and the maximum temperature variation $\widehat{\Delta T}_\xi(t)$ of the cell itself, see Table 7. Both temperature ranges, $\widehat{\Delta T}_{\infty,\xi}(t)$ and $\widehat{\Delta T}_\xi(t)$, are related to room temperature, i.e. $T_\infty = 298\,K$, as a reference.

The parameter identification is started with one experiment $\xi = 1$. Then additional measurements $\xi = 2, \ldots, 5$ are added. This procedure successively increases the number of identifiable parameters according to Eq. (23), see the corresponding group assignment in Table 8. The last three columns of Table 8 show that an addition of measurements, i.e. from $\sum_{\xi=1}^{4}$ to $\sum_{\xi=1}^{5}$, does not further increase the number of parameters in the first group from a certain point on.

Table 8
Group assignment of parameters w.r.t. the test Eq. (23).

$\sum_\xi$ of experiments conducted	1	2	3	4	5
$E_{0,a}$	18	1	1	1	1
$E_{0,c}$	4	1	1	1	1
$E_{0,l}$	15	1	1	1	1
R_a	16	2	1	1	1
R_c	2	2	2	2	2
$D_{s,a}$	10	1	1	1	1
$D_{s,c}$	1	1	1	1	1
ϵ_a	1	1	1	1	1
ϵ_c	1	1	1	1	1
rka_a	19	3	3	2	2
rka_c	5	1	1	1	1
κ	6	1	1	1	1
D_{el}	9	1	1	1	1
h_{tc}	12	1	1	1	1
ϵ_{rad}	14	2	2	2	2
c_0	8	2	2	1	2
$a_{a,1}$	1	2	1	1	1
$a_{c,1}$	2	2	2	2	2
$a_{c,2}$	1	1	1	1	1
$a_{c,3}$	1	1	1	1	1
$a_{c,3+1}$	1	1	1	1	1
$a_{c,3+2}$	2	1	1	1	1
$a_{c,4}$	2	2	2	2	2
$a_{c,4+1}$	1	1	1	1	1
$a_{c,4+2}$	1	1	1	1	1
$a_{c,5}$	2	2	2	2	2
$a_{c,5+1}$	1	1	1	1	1
$a_{c,5+2}$	1	1	1	1	1
β	7	3	2	1	1
γ_a	17	5	1	1	2
γ_c	11	3	3	1	2
δ_a	13	4	1	1	1
δ_c	3	1	1	1	1
Dimension of $\boldsymbol{\theta}_{1st}$	11	20	24	27	24
No. of groups	19	5	3	2	2

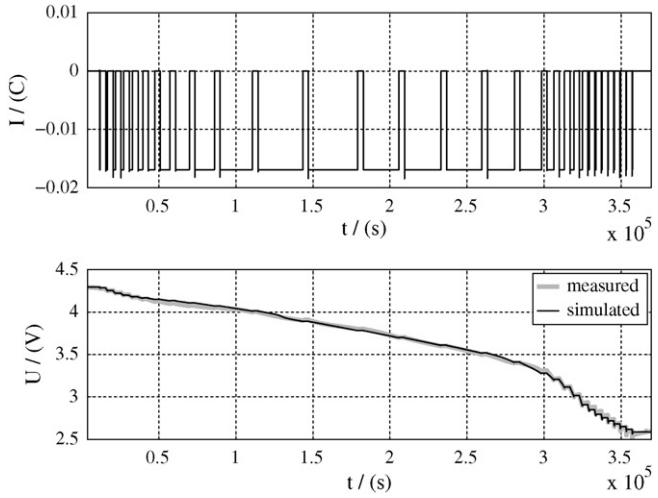

Fig. 4. Pulsed low-rate discharge of the cell with intermediate relaxation phases.

The group assignment listed in Table 8 shows that the uncertainty of a number of parameters is slightly above the test criterion Eq. (23), they remain in the second group. Since an easing of the test criterion would decrease the overall estimation quality, the authors decided to leave these parameters at their initial values. Since the identifiability of parameters is dependent on system stimuli, the sensitivity of these parameters could be improved by a respective design of experiments [31].

The plots shown in Figs. 4–9 have been obtained with one unique set of 33 parameters computed by the identification of the five different experiments according to Tables 7 and 8.

5.2. Comparison of model simulations and real cell experiments

The comparison of the identified cell model Eqs. (11) and (12) is conducted with the measurement data of the experiments ξ as listed in Table 7. The focus is on discussing phenomenologically interesting excerpts of the experiments ξ of Table 7 rather than on the stringent explanation of all profiles $\xi = 1$–5.

5.2.1. Operating the cell in a very low current regime

First, a long-term pulsed discharge of the cell with $I(t) = C/60$ and intermediate rest phases was conducted, as shown in Fig. 4. Within this experiment, mainly the open-circuit behavior of the cell and the slow solid phase diffusion processes can be observed very well. Since the heat generation is negligible at $I(t) = C/60$, the temperature development was not recorded. The ambient temperature T_∞ was fixed at 295 K in the laboratory. During the relaxation phases, i.e. $I(t) = 0$, the diffusive balancing processes inside the active materials are visible. Moreover, the two time constants of the voltage relaxation vary with the $\overline{SOC}_j$. The SOC-dependent diffusion coefficients found for the anode and cathode active materials according to Eq. (8) are depicted in Fig. 3.

5.2.2. Operating the cell at varying ambient temperature levels

In order to investigate the cell behavior over a wide range of the ambient temperature, the stimulation of the cell was extended by $T_\infty(t)$ as an additional manipulated variable, as shown in Fig. 5. The current input was kept in a moderate regime. The temperature development $T(t)$ of the identified model is delayed to the one of the measured cell, as the bottom plot in Fig. 5 shows. Further temperature modeling and also experimental improvements are therefore necessary in order to yield an increased prediction quality. This will be done in future work.

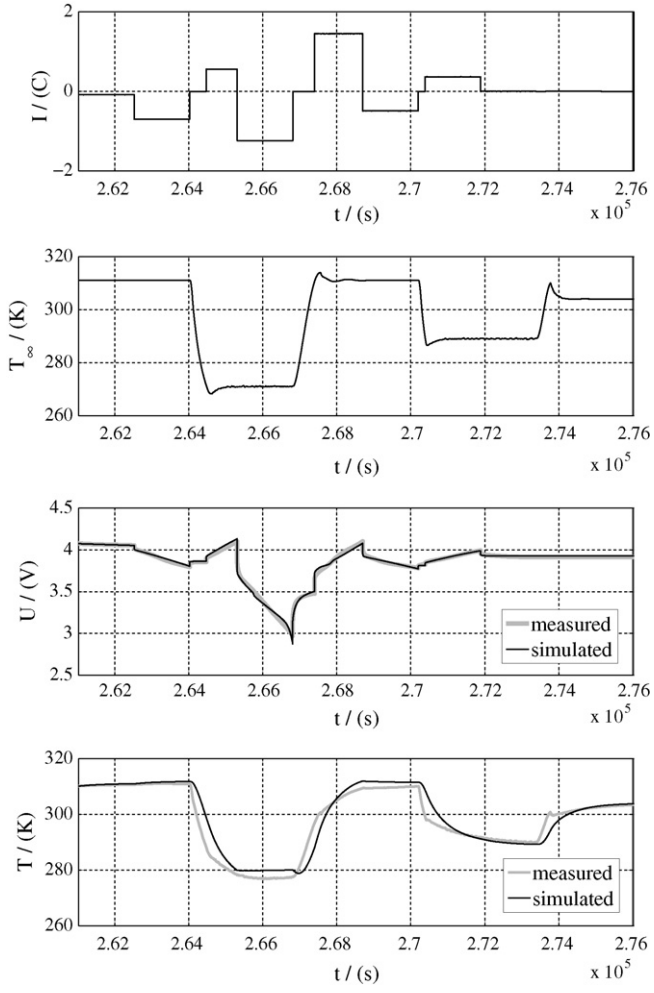

Fig. 5. Current $I(t)$ and ambient temperature $T_\infty(t)$ as manipulated variables.

5.2.3. Operating the cell under potentiostatic conditions

The most common way to charge a secondary lithium-ion battery is the so-called constant current-constant voltage (CCCV) procedure as outlined in [19], where the cell is driven in a galvanostatic regime, i.e. $I(t) = \text{const.}$, until the upper cut-off voltage U_{upper} is reached, see Fig. 6. The terminal voltage $U(t)$ is then controlled w.r.t. the set-point $U(t) = U_{\text{upper}}$. Consequently, the current $I(t)$ decays with time until a pre-defined threshold is reached. The cell is considered fully charged when the current $I(t)$ falls below a lower boundary of $\approx 0.1C$ in the CV phase. Thus, the performance of the model under potentiostatic operating conditions can be investigated by the comparison of a measured CV phase and the respective open-loop simulation, as shown in Fig. 6.

5.2.4. Conducting the manufacturer's standard test profile

The standard test for the investigated lithium-ion cell includes the cycling of the device with an $8C$ discharge followed by a $3C$–$4.1V$–CCCV charge section, see Fig. 7. The cell undergoes a self-heating of approximately 35 K during the discharge phase. Since the profile was recorded twice within the same experiment, a typical behavior of secondary lithium cells is shown in Fig. 7: The shape of the $8C$ discharge terminal voltage curve is different at each cycle. This is not a matter of measurement errors or uncertainties, but the result of reversible degradation. Therefore, a pre-cycling with just this profile was conducted before recording the experiments $\xi = 1$–5 in order to guarantee a reproducible input/output behavior of the cell. It was observed that the shape of the terminal voltage

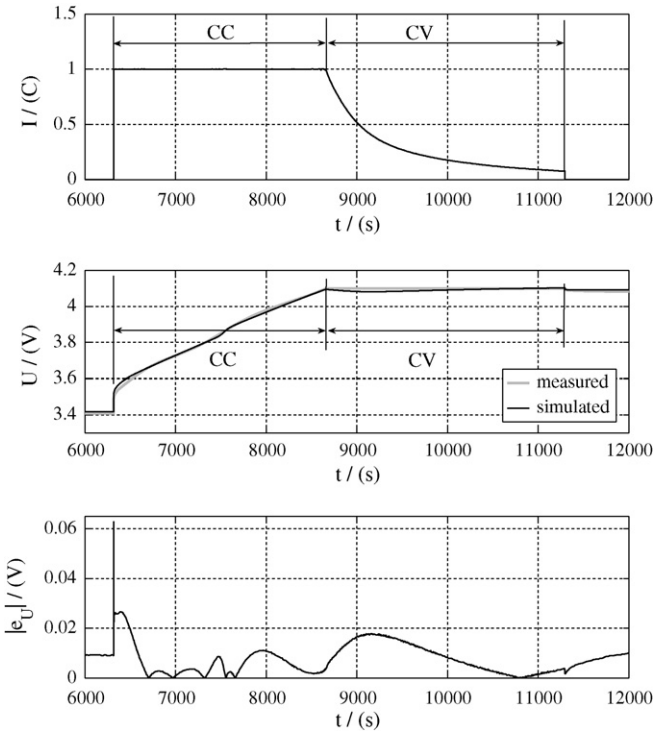

Fig. 6. Current profile during a CCCV charge and the resulting absolute voltage error $|e_U|$ between the measured cell and the model.

curve during discharge continues to change within 5–10 so-called wake-up cycles. Two of them are depicted in Fig. 8. A similar effect of history-dependent charge and discharge behavior was recently reported in [53], but in context with another cell chemistry.

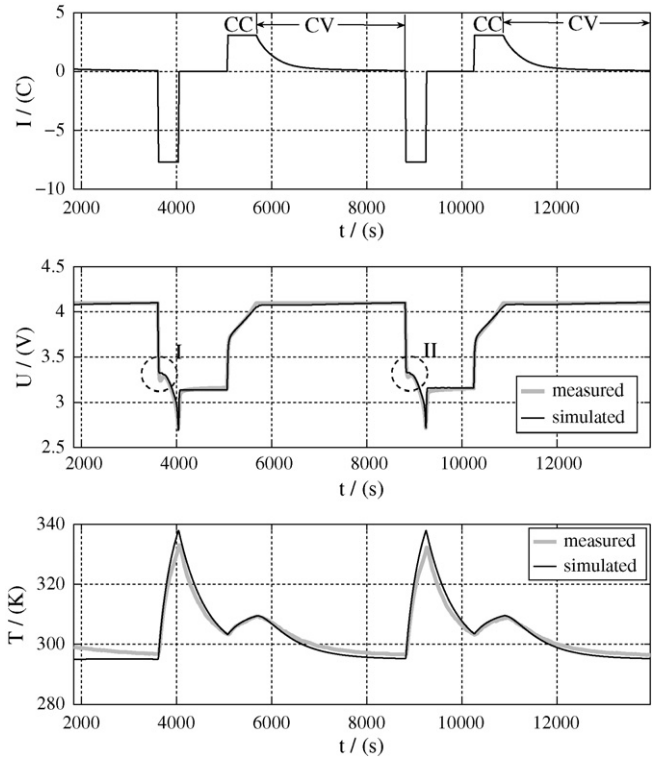

Fig. 7. Standard test cycle of the manufacturer. An 8*C* discharge phase is followed by a CCCV charge.

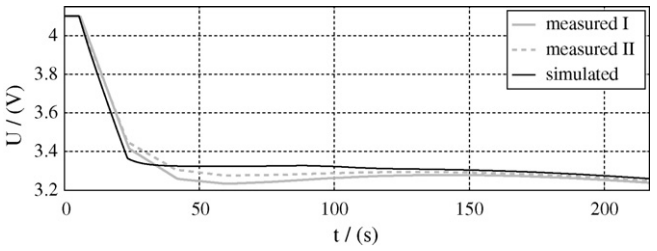

Fig. 8. Zoom of the windows I and II of the center part of Fig. 7. Reversible degradation is observed within the first 5–10 cycles after a longer rest phase.

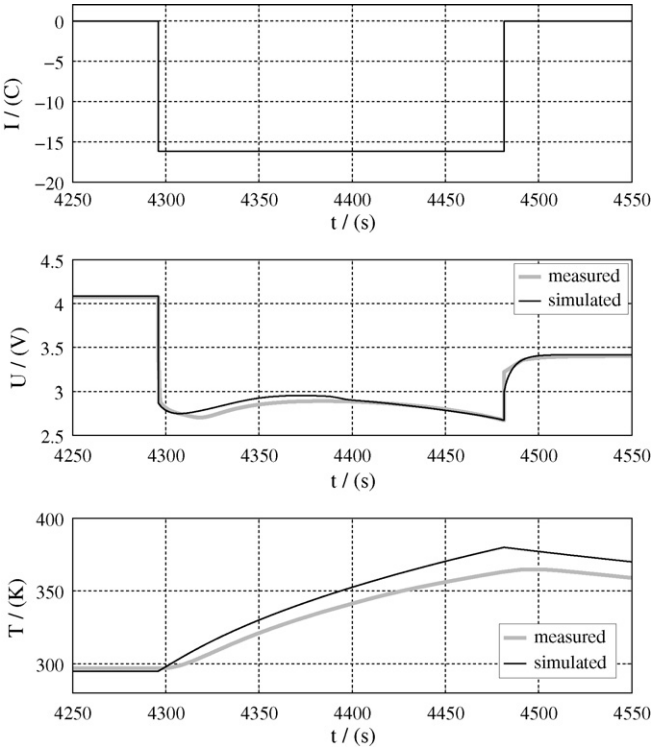

Fig. 9. Maximum-rate discharge. A current $I(t) = 16C$ discharges the cell within less than 3 min.

5.2.5. *Operating the cell with maximum discharge current*

The maximum applied discharge current of $I(t) = 16C$, as shown in Fig. 9, not only causes a harsh voltage drop but also heats the cell by more than 60 K within approximately 3 minutes. The ambient temperature is maintained at $T_\infty = 295$ K. The instantaneous voltage drop is followed by a relaxation unless the current is kept at 16*C*. This is caused by the self-heating of the cell, see Section 3.3. The result is an effectively lowered internal resistance (i.e. faster kinetics) leading to a higher terminal voltage even though the SOC decreases continuously.

6. Summary and conclusion

The incorporation of the most relevant physical effects into a lumped parameter electrochemical lithium-ion cell model was proposed. This procedure yields an excellent reproduction of a real battery's transient and static input/output behavior even though the input is varied by three orders of magnitude. Nevertheless, a simple and real-time capable model structure is maintained. Utilizing the combined parameter analysis and identification, a small set of experiments is chosen. These few measurements allow the proper parameterization for the whole operating range of the device under test. Summarizing the presented work, the proposed

model is a promising candidate for the implementation in onboard battery control units. This is due to its small simulation time of a few seconds on a PC and quick adaptability to various chemistries of intercalation cells. The inherent physical parameters build a profound basis for the incorporation of reversible and irreversible degradation effects. The latter is unavoidable for sophisticated practical applications.

Acknowledgements

We thank Steffen Benzler and Özgür Can Celik for their contributions to this publication in the course of their diploma [38] as well as master thesis [54]. The support by Heiko Pape, Jörg Pöhler and Bernd Aupperle during cell experiments is acknowledged. This work was funded by Robert Bosch GmbH, Stuttgart.

Appendix A. Reference model equations

The following set of equations was first proposed in [5] whereas the theoretical background can be found in [4,55] for instance. A solid phase mass balance for the lithium-ion concentration $c_{1,j}(z, r, t)$ along the radii of the particles is given by

$$\frac{\partial c_{1,j}}{\partial t} = D_{s,j} \cdot \left(\frac{\partial^2 c_{1,j}}{\partial r^2} + \frac{2}{r} \cdot \frac{\partial c_{1,j}}{\partial r} \right) \tag{A.1}$$

with the boundary conditions $\partial c_{1,j}/\partial r|_{r=0} = 0$ and $\partial c_{1,j}/\partial r|_{r=R_j} = -D_{s,j}/j_j$. In the electrolyte phase, the mass balance for lithium-ion concentration $c_{2,j}(z, t)$ is determined by

$$\frac{\partial c_{2,j}}{\partial t} = \frac{1}{\epsilon_j} \cdot \frac{\partial}{\partial z} \left(D_j \cdot \frac{\partial c_{2,j}}{\partial z} + \zeta \cdot i_{2,j} \right) \tag{A.2}$$

with the boundary conditions $\partial c_{2,j}/\partial z|_{z=0,h_{\text{tot}}} = 0$. The constant ζ is defined as $\zeta = (1 - t_+^0)/F$. The corresponding solid phase potential $\Phi_{1,j}(z, t)$ is found as

$$0 = -\frac{\partial \Phi_{1,j}}{\partial z} + \frac{1}{\sigma_j} \left(i_{2,j} - \frac{I(t)}{A_{el}} \right) \tag{A.3}$$

and the electrolyte phase potential $\Phi_{2,j}(z, t)$ is given by

$$0 = -\frac{\partial \Phi_{2,j}}{\partial z} - \frac{i_{2,j}}{\kappa} + RT\,\zeta \left(1 + \frac{\partial \ln f_j}{\partial \ln c_{2,j}} \right) \frac{\partial}{\partial z} \left(\ln c_{2,j} \right). \tag{A.4}$$

The spatial current distribution $i_{2,j}(z, t)$ is calculated by means of the local reaction rate $j_j(z, t)$ and reads as

$$0 = -\frac{\partial i_{2,j}}{\partial z} + a_{s,j}\, F\, j_j, \tag{A.5}$$

where $a_{s,j}$ is the active surface area. The charge transfer is described by the Butler–Volmer reaction kinetics

$$0 = j_j - \frac{s_i}{n} i_{0,j} \left[\exp(-\alpha_c \chi_j) - \exp(\alpha_a \chi_j) \right] \tag{A.6}$$

with the transfer coefficients α_j and the arguments $\chi_j(z, t)$ according to

$$\chi_j = \frac{F}{RT} (\Phi_{1,j} - \Phi_2 - U_{\text{ocp},j} - R_{SEI,j} \cdot j_j), \tag{A.7}$$

where $i_{0,j}(z, t)$ is the exchange current density.

Appendix B. Terminal voltage, state of charge and power capability

According to [5], the terminal voltage of the cell is determined by the solid phase potential difference, i.e.

$$U(t) = \Phi_{1,c}(z = h_{\text{tot}}, t) - \Phi_{1,a}(z = 0, t). \tag{B.1}$$

With the common assumption of equal transfer coefficients, i.e. $\alpha_a = \alpha_c = 0.5$ [4–6,44], Eq. (A.6) can be solved explicitly for $\Phi_{1,j}$ [56], i.e.

$$\Phi_{1,j}(t) = U_{\text{ocp},j}(SOC_j) + \Phi_{2,j}(c_{2,j}, I(t)) - \frac{2RT}{F} \operatorname{Arsinh}\left(\frac{R_j}{2\, i_{0,j}(c_{1,j}, c_{2,j})\, F\, h_j\, a_{s,j}\, A_{el}} I(t) \right), \tag{B.2}$$

where the term $i_{0,j}(c_{1,j}, c_{2,j}, rka_j)$ denotes the exchange current density. The variable $U_{\text{ocp},j}(SOC_j)$ is the open circuit potential of the respective electrode, which is proposed as

$$U_{\text{ocp},j} = a_{j,1} - a_{j,2} \cdot SOC_j - \sum_{i=1}^{N_{\text{ocp}}} a_{j,3i} \cdot \tanh\left(\frac{SOC_j - a_{j,3i+1}}{a_{j,3i+2}} \right), \tag{B.3}$$

with the constant coefficients $a_{j,i}$. In contrast to [8], the sole usage of structurally identical tanh terms for both electrodes guarantees a strict monotonicity for the empiric approach Eq. (B.3). Furthermore, by the appropriate choice of the coefficients $a_{j,i}$ the impact of single summands is limited to a specified SOC range. This fact ensures a unique solution of the parameter estimation task as formulated in Section 4. For reasons of simplicity $U_{\text{ocp},a}$ was fixed to the shape of a typical mesocarbon microbead (MCMB, a graphitic carbon) anode [50] and thus was excluded from the identification.

The particle surface lithium-ion concentration $c_{1,s,j}$ in Eq. (2) denotes the short-term state of charge as

$$SOC_j = \frac{c_{1,s,j}}{\hat{c}_j}, \tag{B.4}$$

which is related to the immediately accessible charge. It can also be regarded as a measure of the currently available power. Here, $\hat{c}_j = C_j\, \rho_j\, a_{s,j}$ is the material-specific maximum concentration. By contrast, the classic definition of *SOC*, e.g. as discussed in [19,57], corresponds to

$$\overline{SOC}_j = \frac{\bar{c}_{1,j}}{\hat{c}_j}, \tag{B.5}$$

where the totally stored charge is considered by means of the averaged lithium-ion bulk concentration $\bar{c}_{1,j}$. For $I(t) = 0$, the surface concentration $c_{1,s,j}, j \in a, c$ settles to the average bulk material concentration $\bar{c}_{1,j}$ according to Eqs. (1) and (2), i.e. $SOC_{j,\text{stat}} = \overline{SOC}_{j,\text{stat}}$. Consequently, the resulting open circuit potential $U_{\text{ocp},j}(c_{1,s,j})$ is a direct measure of the residual amount of stored charge for a cell in the relaxed condition of $dU(t)/dt = 0$ and $I(t) = 0$.

Appendix C. Modal solution of the electrolyte lithium-ion concentration

Assuming that $\epsilon := \epsilon_a = \epsilon_s = \epsilon_c$ and $D := D_a = D_s = D_c$, the expression in Eq. (A.2) can be rewritten as

$$\frac{\partial c_2}{\partial t} = \frac{1}{\epsilon} D \frac{\partial^2 c_2}{\partial z^2} + \frac{\zeta}{\epsilon} \frac{\partial i_2}{\partial z} \tag{C.1}$$

with $z \in (0, h_{\text{tot}})$, see Fig. 1, the boundary conditions of Eq. (A.2), and the initial condition $c_2(z, 0) = c_{2,0}(z)$. Eq. (C.1) can be solved analytically utilizing a modal transformation [21] as described in the following. The modal transformation is defined as

$$c_{2,k}^*(t) = \int_0^{h_{\text{tot}}} \psi_k(z) \cdot c_2(z, t)\, dz, \; k = 0, 1, 2, \ldots \tag{C.2}$$

with the adjoint spatial eigenfunction $\psi_k(z)$ [58]. Applying Eq. (C.2) to Eq. (C.1), one obtains

$$\underbrace{\int_0^{h_{\text{tot}}} \psi_k \frac{\partial c_2}{\partial t} dz}_{dc_{2,k}^*/dt} = \frac{D}{\epsilon} \int_0^{h_{\text{tot}}} \psi_k \frac{\partial^2 c_2}{\partial z^2} dz + \frac{\zeta}{\epsilon} \underbrace{\int_0^{h_{\text{tot}}} \psi_k \frac{\partial i_2}{\partial z} dz}_{=: i_{2,k}^*(t)}. \tag{C.3}$$

The subsequent dual partial integration of the second term in Eq. (C.3) leads to

$$\int_0^{h_{\text{tot}}} \frac{D}{\epsilon}\psi_k(z)\cdot\frac{\partial^2 c_2}{\partial z^2}dz = \lambda_k\psi_k^*(t) \tag{C.4}$$

with the boundary conditions $\partial c_2/\partial z|_{z=0,h_{\text{tot}}} = 0$ and $\partial\psi_k/\partial z|_{z=0,h_{\text{tot}}} = 0$ according to the boundary conditions of Eq. (A.2). The variable λ_k denotes the spatial eigenvalues as proposed in [21]. Hence, in modal coordinates $c_{2,k}^*$, $k\in\mathbb{N}_0$, Eq. (C.1) is equivalent to an infinite-dimensional system of ODEs, i.e.

$$\frac{dc_{2,k}^*}{dt} = \lambda_k c_{2,k}^*(t) + \frac{\zeta}{\epsilon}i_{2,k}^*(t), \qquad t>0 \tag{C.5}$$

with the modal inputs $i_{2,k}^*$ specified in Eq. (C.3) and the modal initial conditions

$$c_{2,k}^*(0) = c_{2,k,0}^* = \int_0^{h_{\text{tot}}} \psi_k(z)\cdot c_0(z)\,dz. \tag{C.6}$$

Eq. (C.5) can easily be solved either analytically or numerically, leading to the solution $c_{2,k}^*(t)$ in the modal domain. The final result is then obtained by conducting the inverse modal transformation according to Eq. (6).

References

[1] Proceedings of the Ninth International Advanced Automotive Battery & EC Capacitor Conference (AABC), Advanced Automotive Batteries, Long Beach, CA, 2009.
[2] Proceedings of the Fifth International Symposium on Large Lithium Ion Battery Technology And Application (LLIBTA), Advanced Automotive Batteries, Long Beach, CA, 2009.
[3] G. Sikha, B. Popov, R. White, J. Electrochem. Soc. 151 (7) (2004) A1114.
[4] J. Newman, K. Thomas-Alyea, Electrochemical Systems, 3rd ed., Wiley-Interscience, Hoboken, NJ, 2004.
[5] M. Doyle, T.F. Fuller, J. Newman, J. Electrochem. Soc. 140 (1993) 1526–1533.
[6] T.F. Fuller, M. Doyle, J. Newman, J. Electrochem. Soc. 141 (1994) 1–10.
[7] T. Fuller, M. Doyle, J. Newman, J. Electrochem. Soc. 141 (4) (1994) 982–990.
[8] M. Doyle, J. Newman, A. Gozdz, C. Schmutz, J. Tarascon, J. Electrochem. Soc. 143 (6) (1996) 1890–1903.
[9] P. Arora, M. Doyle, R. White, in: S. Surampudi, R. Marsh (Eds.), Lithium Batteries Symposium, vol. 98, ECS, Pennington, 1999, pp. 553–572.
[10] G. Botte, V. Subramanian, R. White, Electrochim. Acta 45 (2000) 2595–2609.
[11] V.R. Subramanian, J.A. Ritter, R.E. White, J. Electrochem. Soc. 148 (2001) E444–E449.
[12] G. Sikha, R. White, B. Popov, J. Electrochem. Soc. 152 (8) (2005) A1682–A1693.
[13] M. Johan, A. Arof, J. Power Sources 170 (2007) 490–494.
[14] S. Santhanagopalan, Q. Guo, R. White, J. Electrochem. Soc. 153 (3) (2007) A198–A206.
[15] B. Haran, B. Popov, R. White, J. Power Sources 75 (1998) 56–63.
[16] S.P. Asprey, S. Macchietto, J. Process Contr. 12 (2002) 545–556.
[17] C. Majer, Parameterschaetzung, Versuchsplanung und Trajektorienoptimierung fuer verfahrenstechnische Prozesse, Fortschritt-Berichte, No. 3/538, VDI Verlag, Duesseldorf, 1998.
[18] M. Bitzer, Parameteranalyse, -identifikation und Versuchsplanung am Beispiel eines Fedbatch-Fermentationsprozesses, student research project, Institute of System Dynamics and Control, University of Stuttgart, Stuttgart, 1996.
[19] A. Jossen, W. Weydanz, Moderne Akkumulatoren richtig einsetzen, 1st ed., Printyourbook, Germany, 2006.
[20] V.R. Subramanian, V.D. Diwakar, D. Tapriyal, J. Electrochem. Soc. 152 (2005) A2002–A2008.
[21] E.-D. Gilles, Systeme mit verteilten Parametern, Oldenbourg, Munich, 1973.
[22] M. Guo, K. Kumaresan, G. Sikha, R.E. White, in: Proceedings of the 213th ECS Meeting, abstract available only, 2008.
[23] A. Schmidt, Simulation and state estimation of Li-ion batteries for HEV applications, Master's thesis, Swiss Federal Institute of Technology (ETH) Zurich, Zurich, 2007.
[24] P. Albertus, J. Christensen, J. Newman, J. Electrochem. Soc. 156 (7) (2009) A606–A618.
[25] H. Mehrer, Diffusion in Solids, 1st ed., Springer, Berlin, 2007.
[26] D. Bernardi, E. Pawlikowski, J. Newman, J. Electrochem. Soc. 132 (1) (1985) 5–12.
[27] E.-U. Schluender, VDI-Waermeatlas, 8th ed., Verein Deutscher Ingenieure, VDI-Gesellschaft Verfahrenstechnik und Chemieingenieurwesen (GVC), 1997.
[28] H.-D. Baehr, K. Stephan, Waerme- und Stoffuebertragung, 3rd ed., Springer, Berlin, 1997.
[29] C.E. Mortimer, U. Mueller, Chemie: das Basiswissen der Chemie, 7th ed., Georg Thieme Verlag, Stuttgart, 2001.
[30] V. Schmidt, Statistik II, Lecture Notes, University of Ulm, Ulm, 2006.
[31] K. Schittkowski, Ind. Eng. Chem. Res. 46 (2007) 9137–9147.
[32] R. Isermann, Identifikation dynamischer Systeme II. Besondere Methoden, Anwendungen, 2nd ed., Springer, Berlin, 1992.
[33] G.C. Goodwin, Identification: Experiment Design, in: System and Control Encyclopedia, Pergamon Press, Oxford, 1987.
[34] L. Ljung, System Identification: Theory for the User, Prentice-Hall, Englewood Cliffs, NJ, 1987.
[35] H.K. Khalil, Nonlinear Systems, 3rd ed., Prentice-Hall, Upper Saddle River, NJ, 2001.
[36] A. Saltelli, K. Chan, E.M. Scott, Sensitivity Analysis, 1st ed., Wiley & Sons, West Sussex, 2000.
[37] S. Koerkel, Numerische Methoden fuer Optimale Versuchsplanungsprobleme bei nichtlinearen DAE-Modellen, PhD thesis, University of Heidelberg, Heidelberg, 2002.
[38] S. Benzler, Kombinierte Parameteranalyse und -identifikation mit optimierungsbasierter Versuchsplanung am Beispiel eines Diesel-Luftsystems und eines Lithium-Ionen-Batterie-Modells, Diploma thesis, University of Stuttgart, Stuttgart, 2008.
[39] A.F. Emery, A.V. Nenarokomov, Meas. Sci. Technol. 9 (1998) 864–876.
[40] A. Munack, C. Posten, at–Automatica 37 (2) (1989) 55–65.
[41] W.G. Mueller, Collecting Spatial Data: Optimum Design of Experiments for Random Fields, 3rd ed., Springer, Berlin, 2007, pp. 43–76.
[42] http://www.wolfram.com/mathematica.
[43] http://www.mathworks.com.
[44] S. Santhanagopalan, Q. Guo, P. Ramadass, R. White, J. Power Sources 156 (2005) 620–628.
[45] K. Smith, C. Rahn, C. Wang, Energy Convers. Manage. 48 (2007) 2565–2578.
[46] D. Abraham, in: M. Broussely (Ed.), Third International Symposia, Large Lithium Ion Battery Technology And Application (LLIBTA), 2nd ed., Advanced Automotive Batteries, USA, 2007.
[47] S. Santhanagopalan, R. White, J. Power Sources 161 (2006) 1346–1355.
[48] D.P. Abraham, S. Kawauchi, D.W. Dees, Electrochim. Acta 53 (2008) 2121–2129.
[49] G. Botte, B. Johnson, R. White, in: S. Surampudi, R. Marsh (Eds.), Lithium Batteries Symposium, vol. 98, ECS, Pennington, NJ, 1999, pp. 526–552.
[50] T. Zheng, J. Reimers, J. Dahn, Phys. Rev. B 51 (1995) 734–741.
[51] H.-D. Joos, MOPS – Multi-objective parameter synthesis user's guide v5.0, User's Guide, DLR, Institut fuer Robotik und Mechatronik, Oberpfaffenhofen, 2007.
[52] M.J.D. Powell, in: A. Iserles (Ed.), Acta Numerica, vol. 7, Cambridge University Press, Cambridge, MA, 1998, pp. 287–336.
[53] M.A. Roscher, J. Vetter, D.U. Sauer, J. Power Sources 191 (2009) 582–590.
[54] C. Celik, Automated parameter identification & optimization based design of experiments for the efficient parameterization of dynamic models of lithium-ion cells, Master's thesis, Hamburg University of Technology (TUHH), Hamburg, 2009.
[55] K. Kumaresan, G. Sikha, R.E. White, ECS Trans. 3 (27) (2007) 173–190.
[56] I.N. Bronstein, K.A. Semendjajew, G. Musiol, H. Muehlig, Taschenbuch der Mathematik, 4th ed., Verlag Harri Deutsch, Frankfurt a.M., 1999.
[57] S. Piller, M. Perrin, A. Jossen, J. Power Sources 96 (2001) 113–120.
[58] R. Courant, D. Hilbert, Methoden der mathematischen Physik, 4th ed., Springer, Berlin, 1993.